Planetary and Space Science 135 (2017) 43–54

Contents lists available at ScienceDirect

Planetary and Space Science

journal homepage: www.elsevier.com/locate/pss

Re-evaluation of Apollo 17 Lunar Seismic Profiling Experiment data

Alexandra Heffels[a,*], Martin Knapmeyer[a], Jürgen Oberst[a,b], Isabel Haase[c]

[a] German Aerospace Center - Institute for Planetary Research, Berlin, Germany
[b] Moscow State University for Geodesy and Cartography (MIIGAiK), 105064 Moscow, Russia
[c] Technical University Berlin, Berlin, Germany

A B S T R A C T

We re-analyzed Apollo 17 Lunar Seismic Profiling Experiment (LSPE) data to improve our knowledge of the subsurface structure of this landing site. We use new geometrically accurate 3-D positions of the seismic equipment deployed by the astronauts, which were previously derived using high-resolution images by Lunar Reconnaissance Orbiter (LRO) in combination with Apollo astronaut photography. These include coordinates of six Explosive Packages (EPs) and four geophone stations. Re-identified P-wave arrival times are used to calculate two- and three-layer seismic velocity models. A strong increase of seismic velocity with depth can be confirmed, in particular, we suggest a more drastic increase than previously thought.

For the three-layer model the P-wave velocities were calculated to 285, 580, and 1825 m/s for the uppermost, second, and third layer, respectively, with the boundaries between the layers being at 96 and 773 m depth.

When compared with results obtained with previously published coordinates, we find (1) a slightly higher velocity (+4%) for the uppermost layer, and (2) lower P-wave velocities for the second and third layers, representing a decrease of 34% and 12% for second and third layer, respectively. Using P-wave arrival time readings of previous studies, we confirm that velocities increase when changing over from old to new coordinates. In the three-layer case, this means using new coordinates alone leads to thinned layers, velocities rise slightly for the uppermost layer and decrease significantly for the layers below.

1. Introduction

1.1. Apollo 17 mission

NASA's early lunar exploration culminated in the sixth manned landing of Apollo 17. The mission was launched on December 7, 1972 and touched down on the lunar surface on December 11, before returning safely to Earth eight days after (Fig. 1).

During their stay on the lunar surface, the astronauts deployed several scientific experiments which represent a unique source of lunar ground truth up to the present day. Among other experiments, they deployed the Apollo 17 Lunar Seismic Profiling Experiment (LSPE) which consisted of an array of four identical geophones of the moving coil type with a natural frequency of 7.5 Hz (Vostreys, 1980), set up in a Y-shaped array (see Fig. 2, p. 4), and a set of eight explosive packages (EP). The eight EPs were built identically except for the amount of explosives used and the securing mechanical timers (Table A1, Appendix). A mixture of HNS (Hexanitrostilbene) and Teflon (90%/10%) was used as explosive substance (Kilmer and Laboratory, 1973). All EPs were detonated remotely after the astronauts had left the lunar surface (Fig. 3).

The purpose of the LSPE was to record seismic waves generated by detonations of the eight EPs, the thrust of the Lunar Module's ascent stage during launch, and upon its impact. In addition, a secondary objective was the monitoring of seismic waves generated by natural events.

1.2 Lunar Reconnaissance Orbiter

In 2009, the Lunar Reconnaissance Orbiter (LRO) mission was launched. From a near-circular polar orbit, LRO Narrow Angle Camera (NAC) mapped the lunar surface at a maximum resolution of 50 cm/pixel. This allowed a detailed mapping of Apollo landing sites and reconstruction of the geometry of the deployed seismic array. Geometrically accurate coordinates (lat /long/heights) were determined by combination of these high-resolution orthoimages with Apollo surface panoramas taken by the astronauts (Haase et al., 2013). With this method it was possible to determine new geometrically accurate coordinates for six of the eight EPs. The positions of EP1 and EP7 could not be determined. Since the images where these devices are seen lack distinctive landmarks, it is not possible to reconstruct their accurate coordinates.

* Corresponding author.

http://dx.doi.org/10.1016/j.pss.2016.11.007
Received 8 July 2016; Received in revised form 26 September 2016; Accepted 24 November 2016
Available online 10 December 2016
0032-0633/ © 2016 The Authors. Published by Elsevier Ltd.
This is an open access article under the CC BY-NC-ND license (http://creativecommons.org/licenses/BY-NC-ND/4.0/).

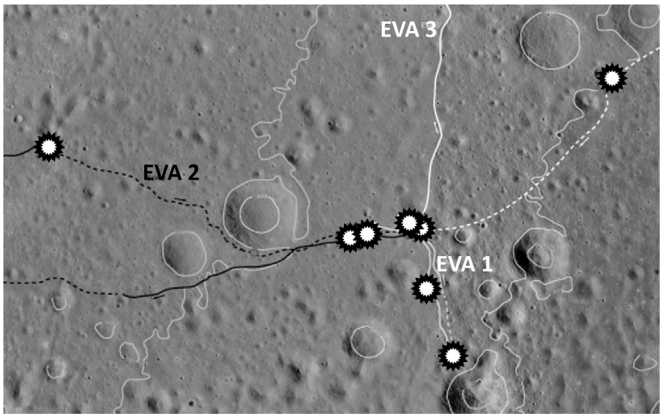

Fig. 1. Mosaic of LROC-images of Apollo 17 landing site with depicted paths for extravehicular activities (EVA) of the astronauts. Stars mark the positions of explosive packages. Some contour lines added to give terrain overview.

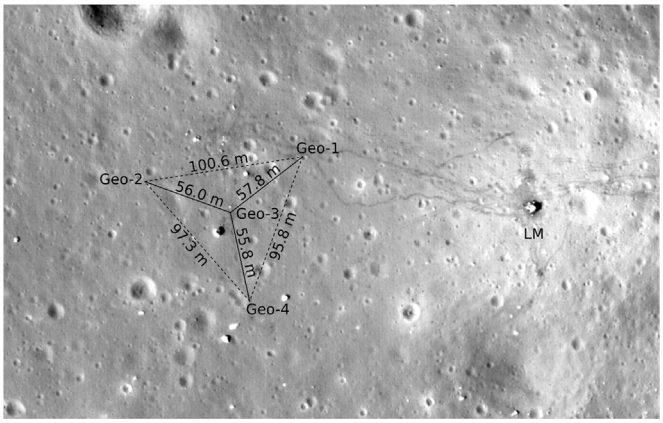

Fig. 2. Apollo 17 landing site with Y-shaped array. Geophone-array with point distances marked. Position of Lunar Module (LM) to the right side of the array. Foot tracks of astronauts are clearly visible between array and LM.

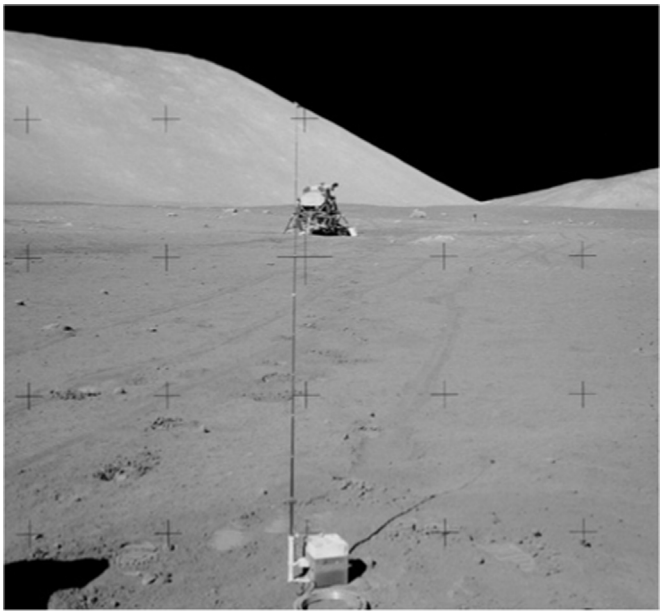

Fig. 3. Picture of EP8 with extended antenna and Lunar Module in the background. Distance between EP8 and Lunar Module approximately 290 m. Size of EP with extended antenna 157.48 cm (NASA, 1972). Astronauts took pictures of the equipment during their extravehicular activities (NASA).

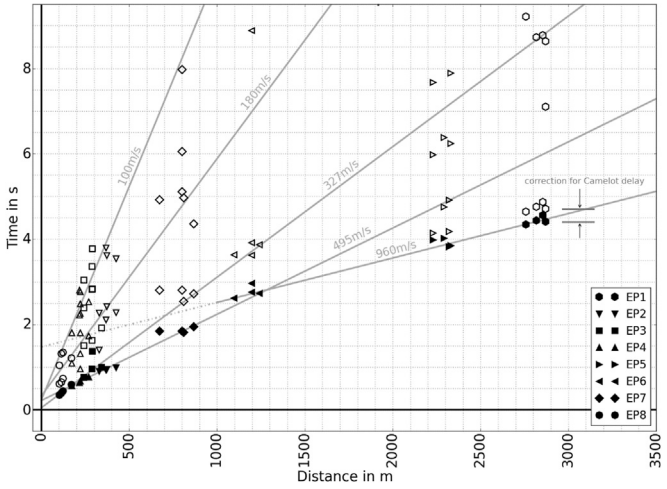

Fig. 4. Apollo 17 travel time curves (Cooper et al., 1974). Original numerical data for P-wave first arrivals was kindly provided by Kovach (pers. communication). Remaining secondary arrival times were digitized from a printed version of the figure 13 in the paper by Cooper et al. (1974). Correction for delay in travel times caused by Camelot crater is marked on right side of the plot. Filled markers depict first arrivals, unfilled markers depict other phase arrivals, grey lines show slopes with the suggested velocities of 100, 180, 327, 495, and 960 m/s.

New LROC-derived coordinates of seismic equipment differ from previously published coordinates by up to 40 m. In addition, the new LROC-derived coordinates include topographic height information (differences in height in the range of 35 m (Haase et al., 2013)) not available before.

In this paper, we re-analyze the seismic data using new seismic arrival time readings and coordinate information to update seismic velocity depth profiles at the Apollo 17 site (Fig. 4).

2 Method

2.1. Cooper model

Cooper et al. (1974) presented a five-layer model with the velocities being 100, 327, 495, 960, and 4700 m/s (Fig. 5). The seismic velocity of the uppermost layer (100 m/s) was adopted from thumper data acquired at the Apollo 14 and 16 sites. Unfortunately, there were no thumper experiments conducted during Apollo 17 mission. The existence of the deepest 4700 m/s layer was inferred from the P-wave arrival times of the Apollo 17 LM impact recorded with the LSPE. Nakamura (2011) proved that there was a timing error in the data and therefore this layer is not existent as stated before. Original P-wave arrivals (plotted, but not listed in early publications) were kindly provided by Kovach (pers. communication, 2015). The numerical values for new and old P-wave arrival times can be found in Table A2 in the appendix. Unfortunately, the associated arrival times of other than first arrivals were not available.

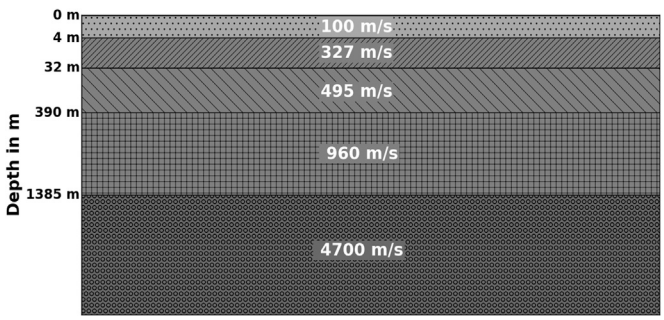

Fig. 5. Depiction of the velocity-depth model from Cooper et al. (1974).

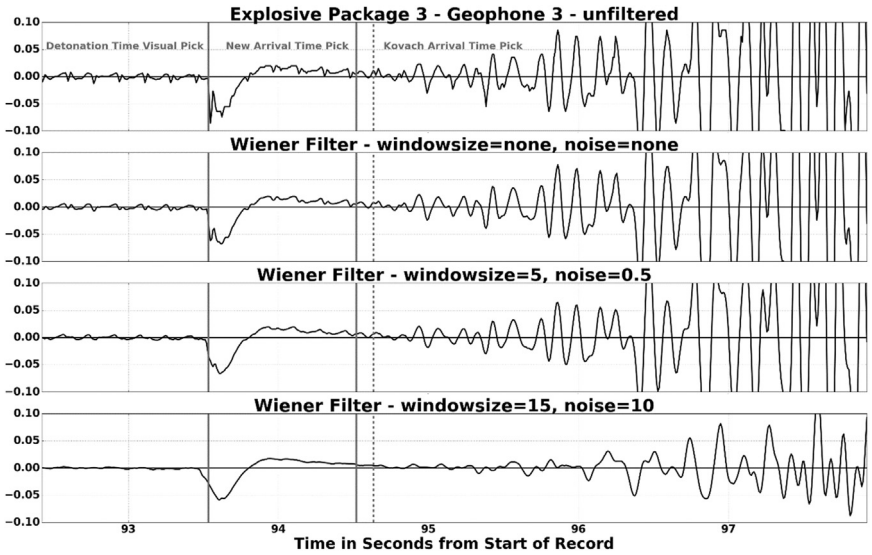

Fig. 6. Seismogram plots of EP3 detonation recorded with geophone 3. The uppermost plot shows raw data. The plots below show different Wiener filters applied to find first arrival picks. The electronic detonation impulse is clearly visible as a strong peak in the data. The bold line marks our visual picks of detonation- and seismic wave arrival times. The dashed line in grey marks the arrival time pick from Kovach (pers. communication, 2015).

2.2. Arrival time readings

Seismic signals traveling within the Moon are affected by strong scattering. Hence, raw seismograms show feature-less spectra, emergent arrivals, and long signal decay times, impeding the identification of secondary phases (Cooper and Kovach, 1975; Duennebier and Sutton, 1974). Furthermore, periodic noise generated by the transmitter contaminated all recorded signals (Cooper et al., 1974). Since, it is almost impossible to identify first arrivals in raw data plots, we had to use different digital techniques to improve visibility of first arrivals. In order to remove possibly occurring trends, the mean of data was subtracted on every single trace. While original data analysis used unspecified prediction error filter, we decided to use a Wiener filter. The Wiener filter is a prediction error filter designed from an autocorrelation function estimated from a short data sample. We varied the size of Wiener filter window from 5 to 15 in each dimension, and the noise-power from an estimated average to fixed values of 0.5 and 10 for the local variance input to find the best fitting approach. The filtered records provided a basis for new readings of P-wave arrival times (see Fig. 6).

2.3. Travel time function and depth profiles

The new Lunar Reconnaissance Orbiter Camera (LROC)-based point distances from Haase et al. (2013) are available for six of the eight Explosive Packages (EPs). Hence, to work with a self-consistent data set we only use the EPs where old and new coordinates are existent. Therefore, we plotted the first arrivals against the distances from the four geophones for the detonations of EP2, EP3, EP4, EP5, EP6, and EP8.

Travel time inversions were carried out using our new arrival time readings in combination with LROC-based point distances from Haase et al. (2013). Previous arrival time (Kovach, 2015) and coordinate data (Cooper and Kovach,1975) were used for comparison.

The combination of old and new coordinates with old and new travel time readings led to four different combinations: (a) new travel time readings from this study with point distances from Haase et al. (2013), (b) new travel time readings with point distances from Cooper and Kovach (1975), (c) old Kovach's travel time readings with point distances from Haase et al. (2013), and (d) old Kovach's travel times readings with point distances from Cooper and Kovach (1975).

As mentioned before Cooper et al. (1974) purposed a five-layer model (Fig. 5). In this model the uppermost layer with a velocity of 100 m/s was derived from Apollo 14 and 16, and the last layer with a velocity of 4700 m/s was proven to be in error by Nakamura (2011). Neglecting these two layers would result in a three-layer model. It was readily apparent that it was possible to fit a straight line through the arrivals from the four closest detonations (EP2, EP3, EP4, and EP8), which represented the first layer in all models. But as mentioned above, we decided to neglected EP1 and EP7 in order to work with a self-consistent data set. In the three-layer case this means that second and third layers are only determined by four points (one EP recorded with all four geophones). Four points may seem to be a small data set to determine a layer. Therefore, we decided to also evaluate EP5 and EP6 as points on one straight line instead of two separated lines. This led to two-layer models. The reciprocal value of the slopes represented the velocity of the layer, while the thicknesses of these layers were calculated from intercept times, using standard equations for refraction seismics (e.g., Telford et al., 1990).

Examination of the residuals, e.g. in lag plots or histograms, served as a quality check for all cases. A random pattern in the residuals would support a linear model, which in this case means that our linear regression model to determine the slopes was sufficiently accurate. This would be supported by a normal distribution in the residuals histogram plots. Additionally, a residual lag plot would serve as a check for randomness in distribution of residuals, proving appropriateness of the regression models used. Residual plots, histogram plots, and residual lag plots can be found in the appendix (Figs. A2-A6).

3 Results

3.1. Two-layer case

(Fig. 7) The velocity and depth of the uppermost layer was well constrained by data from four EPs (EP2, EP3, EP4, and EP8) recorded by all four geophones. For the velocity of the second layer only detonations of two charges (EP5 and EP6) were taken into account.

When using our new arrival time readings and new LROC-based coordinates, we find velocities of 285 and 775 m/s for the two layers, respectively, with the depth of the first layer at 170 m. Using the early travel time readings from Kovach (pers. communication, 2015), we obtained velocities of 320 and 1150 m/s for the first and second layer, respectively, with the transition between the two layers at 324 m.

For comparison we also used the previous coordinates from Cooper

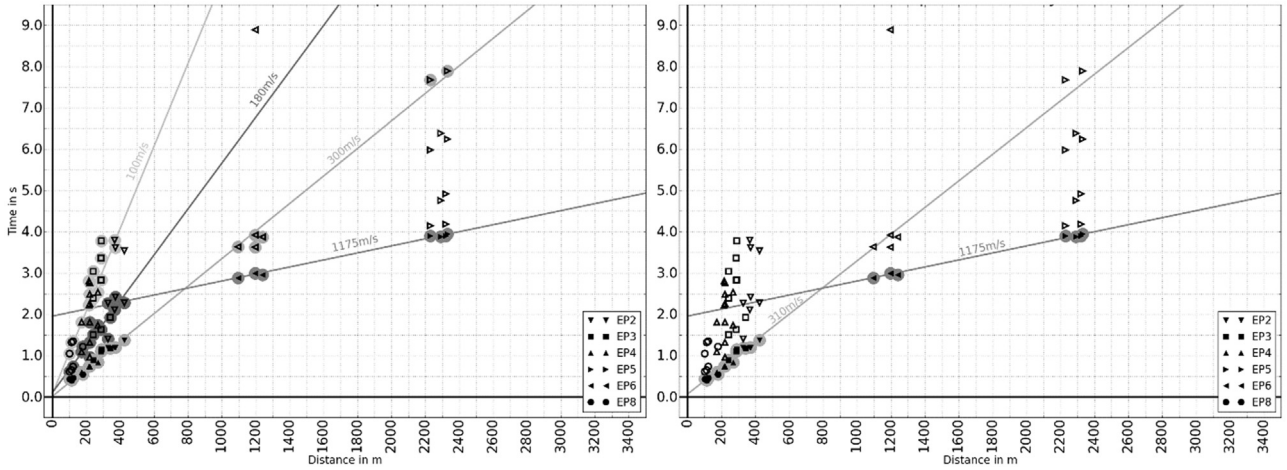

Fig. 7. Comparison of data points and fitted linear travel time functions. Only points of the self-consistent data set are depicted here, this means points of EP1 and EP7 are not shown. Points with background circles used for slope determination. Filled markers depict first arrivals, unfilled markers depict other phase arrivals, grey lines show new calculated slopes. Original numerical data for P-wave first arrivals was kindly provided by Kovach (pers. communication, Table A2 in appendix). Remaining other phase arrival times were digitized from a printed version of the figure 13 in the paper by Cooper et al. (1974). Left: Lines were fitted through all suitable points irrespective of phase. Right: Lines were fitted only through first arrival points. Fitting lines through the new obtained points for first and later phase arrivals leads to velocities of 100, 180, 300, and 1175 m/s if all different phase arrivals are used (left side). When using first arrivals only, the two lowest velocity slopes for 100 and 180 m/s cannot be detected since these are solely constrained by later phase arrivals (right side). This means, neglecting points of EP1, EP7, and the LM impact favors a two layered model.

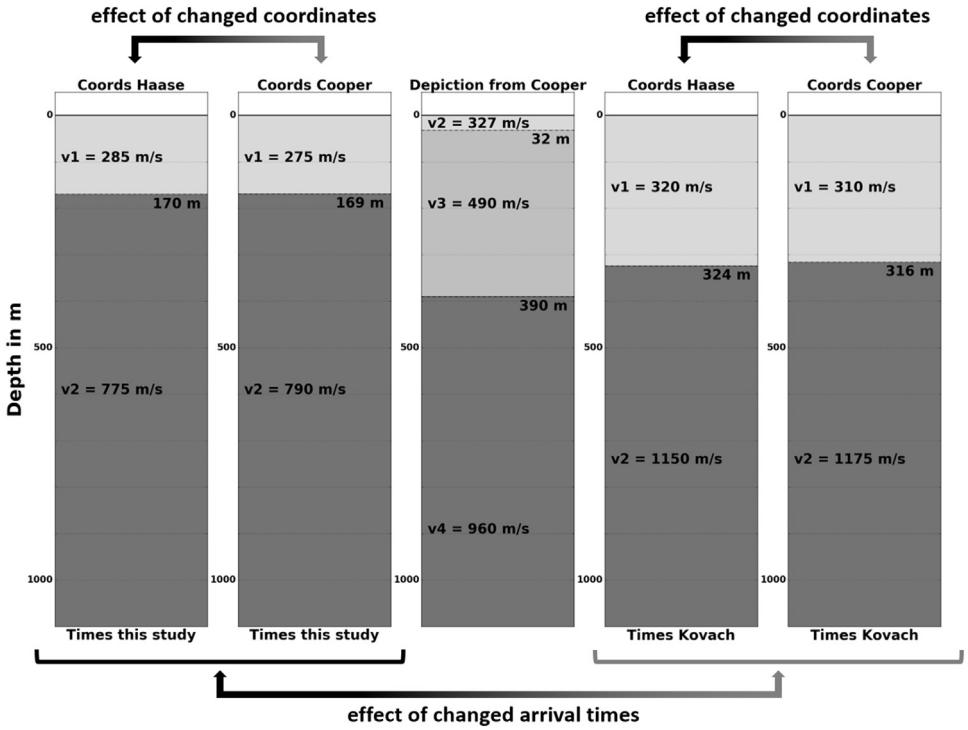

Fig. 8. Comparison of depth models for the two-layer case. The column in the middle represents the velocity-depth profile of Cooper et al. (1974); for better readability of the figure the uppermost 100 m/s-layer with a thickness of 4 m and the lowest 4700 m/s-layer at a depth of 1385 m depth are not depicted here. Left side columns were generated with new travel time readings from this study. Right side columns were generated with travel time readings from Kovach (pers. communication, 2015). For better readability no error bars are denoted in this plot. In the two-layer case, almost no change in layer thickness is observable when changing over from old to new coordinates. Trends in the velocity changes are equal to the three-layer case: velocities slightly rise for the uppermost layers. In contrast, P- wave velocities for the layer below decrease.

and Kovach (1975) in combination with our new arrival time readings. In this case the velocities of the layers were 275 and 790 m/s for the first and second layer, respectively, and a layer boundary at 169 m. Using the Kovach travel time readings, this led to velocities for the first and second layer of 310 and 1175 m/s, respectively, and a transition at a depth of 316 m (see Fig. 8).

Evaluating the residuals, the histogram of residuals, and the residual lag plot for each of the four cases showed that for both layers the variance of the residuals is constant and the histograms of the residuals showed a normal distribution (appendix, Figs. A2 and A3). And, the random errors were independent from each other as shown in the residual lag plots (appendix, Figs. A2 and A3, lower panels).

We used these plots for calculating a set of depth profiles, shown in Fig. 8.

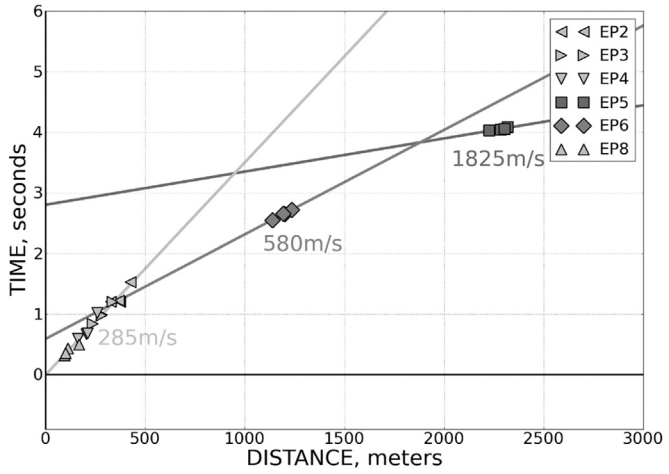

Fig. 9. Travel time plot for data from this work. The light grey line represents the best fitting line through data points of EP2, EP3, EP4, and EP8. The reciprocal slope of this line gives a P-wave velocity of 285 m/s. Best fitting lines for EP6 and EP5 are depicted in separated lines. These slopes lead to P-wave velocities of 580 m/s for the second layer and 1825 m/s for the third layer.

3.2. Three-layer case

Again, the velocity and depth of the uppermost layer was well constrained by data from four EPs (EP2, EP3, EP4, and EP8) recorded by all four geophones. However, for the second layer (which includes velocity and depth) and the velocity of the third layer only one single shot was taken into account, respectively.

When the new travel time readings were combined with the coordinates by Haase et al. (2013) the P-wave velocities were 285 m/s, 580 m/s, and 1825 m/s for first, second, and third layer, respectively, with transitions between the layers at depths of 96 and 773 m (Fig. 9). In contrast, when the new arrival time readings from this study and the coordinates of Cooper and Kovach (1975) were used in combination, we obtained the velocities as 275 m/s, 876 m/s, and 2073 m/s for first, second, and third layer, respectively, and transitions between the layers at depths of 188 and 986 m.

For comparison, we calculated the velocities depth models with travel time readings from Kovach (pers. communication, 2015). When combining the old travel time readings from Kovach with the Haase et al. (2013) coordinates, the P-wave velocities were 322, 1053, and 2750 m/s for first, second, and third layer, respectively. The transitions between the layers were calculated to depths of 310 and 1022 m. When combining Kovach's travel time readings with the early coordinates from Cooper and Kovach (1975), these velocities were 315, 1410, and 3155 m/s for first, second, and third layer, respectively, with layer boundaries at depths of 340 and 1174 m.

Evaluation of the residuals, the histogram of residuals, and the residual lag plot for each of the four cases showed that for all three layers the residuals were evenly distributed above and below the reference line at 0. The histograms of the residuals showed a normal distribution. And, the random errors were independent from each other as shown in the residual lag plots (see appendix, Figs. A4–A6).

4 Discussion

Further improvements to our models may become available, if positions of EP1, EP7 and the Lunar Module (LM) impact can be found. Identification of EP1 and EP7 in images from current lunar spacecraft is not likely. LRO is currently moving in a "frozen orbit" at higher altitude than in its early mission, from where landing site studies at the previous high image resolution is not possible. Hence, we must await mapping of Apollo landing sites by future missions with imaging from more favorable orbits. From our modeling, EP7 and EP1, appear to lie in the transition for the first/second layer and the second/third layer, respectively. Including the missing position data of EP1, EP7, and the LM impact will help to determine more precisely the transitions between the three layers, and the seismic velocity structure beneath the Apollo 17 landing site.

When analyzing lunar farside deep moonquakes for investigation of the deep lunar interior, Nakamura (2005) noticed that the featureless spectra of lunar seismograms makes them hard to read and different seismologists working on the same data set will pick different times for first arrivals. It is likely to be similar with the investigations of this study. Hence, variations in total values are hard to compare but trends can be observed and will be discussed below. For both, the two- and three-layer case, we see that P-wave velocities for the upper layer become larger, when new coordinates are used, whereas P-wave velocities for lower layers decrease significantly.

4.1. Two-layer case

In the two-layer case, when using coordinates from Cooper and Kovach (1975) velocities of uppermost layers are lower whereas velocities of second layers are higher than results calculated with new LROC-derived coordinates from Haase et al. (2013). For coordinates by Cooper and Kovach (1975) we calculate the P-wave velocities of uppermost layers to be 310 and 275 m/s for arrival time picks from Kovach (pers. communication, 2015) and from this study, respectively. For second layers the P-wave velocities can be calculated to be 1175 and 790 m/s for old and new arrival time picks, respectively. When using coordinates from Haase et al. (2013), P-wave velocities of uppermost layers are higher (+10 m/s) and for second layers lower (−25 m/s for early Kovach arrival time picks and −15 m/s for arrival time picks from this study). The layer thickness remains almost constant when using one set of arrival time picks irrespective of coordinates used (see Fig. 8).

Regardless of the travel times used, the velocities were only slightly higher for uppermost layers but dropped significantly for other layers when using new instead of early coordinates.

4.2. Three-layer case

When using coordinates from Cooper and Kovach (1975) velocities of uppermost layers are lower whereas velocities of second and third layers are significantly higher than in the case of new LROC-derived coordinates from Haase et al. (2013). For Cooper's coordinates we calculate the P-wave velocities of uppermost layers to be 310 and 275 m/s for arrival time picks from Kovach (pers. communication, 2015) and from this study, respectively. For second layers the P-wave velocities can be calculated to be 1174 and 876 m/s for old and new arrival time picks, respectively, and for third layers the P-wave velocities are 3155 and 2074 m/s for old and new arrival time picks, respectively (see Fig. 10).

When using coordinates from Haase et al. (2013), P-wave velocities of uppermost layers are slightly higher (+7 and +10 m/s for old and new arrival time picks, respectively) and for second and third layers significantly lower. Second layer velocities drop to 1053 and 580 m/s for old and new arrival time picks, respectively, and third layer velocities drop to 2750 and 1825 m/s for old and new arrival times picks from this study, respectively. Regardless of the travel times used, the velocities raised little for uppermost layers but dropped significantly for second and third layers when changing over from old to new coordinates.

The layer thicknesses are reduced clearly when using the new LROC-derived set of coordinates. Additionally, the layer thicknesses of all layers are reduced significantly when using the set of arrival time picks from this study (e.g. layer thickness of uppermost layer is reduced from 310 to 96 m which represents a reduction by approx. 70%).

We confirm a strong increase of seismic velocity with depth. In our

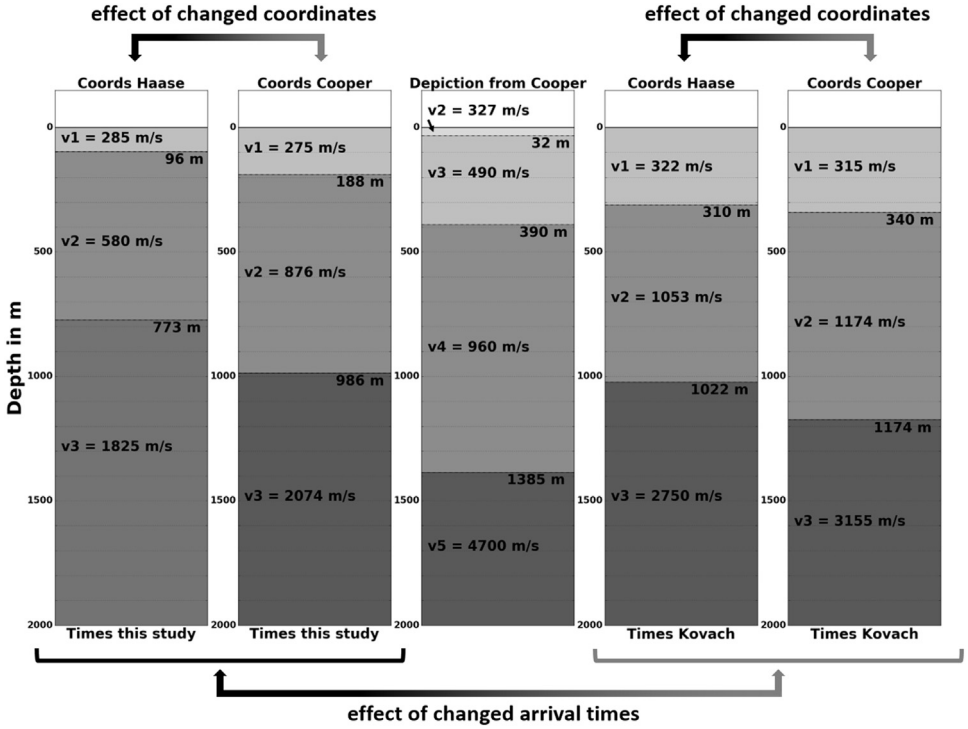

Fig. 10. Comparison of depth models for the three-layer case. Chart in the middle represents a depiction of the depth profile published in (Cooper et al., 1974), the uppermost 100 m/s-layer with a thickness of 4 m is not depicted here. Left side charts generated with new travel time readings from this study. Right side charts generated with travel time readings from Kovach (pers. communication, 2015). For better readability no error bars are denoted in this plot. Changing over from old to new coordinates results in a thinning of layers. Velocities slightly rise for the uppermost layers. In contrast, p- wave velocities for lower layers decrease significantly.

new model, upper layers tend to be thinner and have lower velocities, leading to more drastic increase of velocity with depth compared to previous analyses (Cooper et al., 1974).

In general, the residual plots do not show any trends. In particular, the histogram plots of the residuals show a normal-distributed variance, and the residual lag plots show a random pattern, suggesting uncorrelated errors, as is pre-required for our regression model. Furthermore, residuals show less scattering and correlation, attesting to the appropriateness of the model (Appendix, Figs. A4-A6).

When using new P-wave arrival time readings from this study in combination with LROC-based coordinates, it is clearly visible that layer thicknesses are reduced compared to the velocity depth model published by Cooper et al. (1974) (Fig. 5).

All models from this study suggest a more drastic increase of seismic velocity with depth. This becomes more clear when comparing the most left and most right columns in Fig. 10, depicting the velocity depth models when using new P-wave arrival times in combination with new LROC-derived coordinates and old arrival time picks of Kovach in combination with old coordinate data from Cooper and Kovach (1975), respectively.

The results from this study may change the view of the structure of the upper lunar crust as depicted in “The Lunar Sourcebook” (Heiken et al., 1991, chapter 4). In their depiction of the upper lunar crust, the top most layer reaches to a depth of only 10 m with sound velocities of lower than 500 m/s, and the layer below with sound velocities between 1000 and 2000 m/s reaches to a depth of $\geq$2000 m. With models from this study, this depiction can be refined. We show that the use of new LROC-derived coordinates alone can set the boundary between layers of 322 m/s and more than 1000 m/s (see Fig. 10, fourth column from the left) to a depth of 310 m. With new arrival time readings from this study this is set to a depth of 96 m as a boundary between layers of 285 m/s and 580 m/s. When using new coordinates and new arrival times readings seismic velocities exceed 1000 m/s not until the boundary to the third layer is reached at a depth of 773 m, where we calculated the velocity to be 1825 m/s. This is possibly implying a higher degree of compaction of the regolith. While one may try to explain these different structures by data from EP1, EP7, and the LM impact or from secondary seismic arrivals (used in the paper by Cooper et al. (1974), but not used here), this study shows that the small differences in arrival time readings do not affect the observed trends when changing over from old to new coordinates. In contrast, it is our coordinate updates that yield significantly different structural models.

Our two-layer structures show good agreement with previously published models (compare Fig. 4). In contrast, for the three layered models, the uppermost layers are thinner, suggesting a more drastic increase in seismic velocity with depth than was previously thought.

Acknowledgements

We like to thank the NSSDC for providing access to the original raw data streams and their friendly support. In addition, we like to thank Matthew Brzostowski and Yosio Nakamura for their great support in deciphering the original Apollo data bit stream and associated data. Furthermore, we like to thank Robert Kovach for sharing his personal notes on the Apollo 17 LSPE. This study is supported by the Helmholtz Alliance “Robotic Exploration of Extreme Environments – ROBEX” (HA-304).

J. Oberst gratefully acknowledges being hosted by MIIGAiK and supported by the Russian Science Foundation under project 14-22-00197.

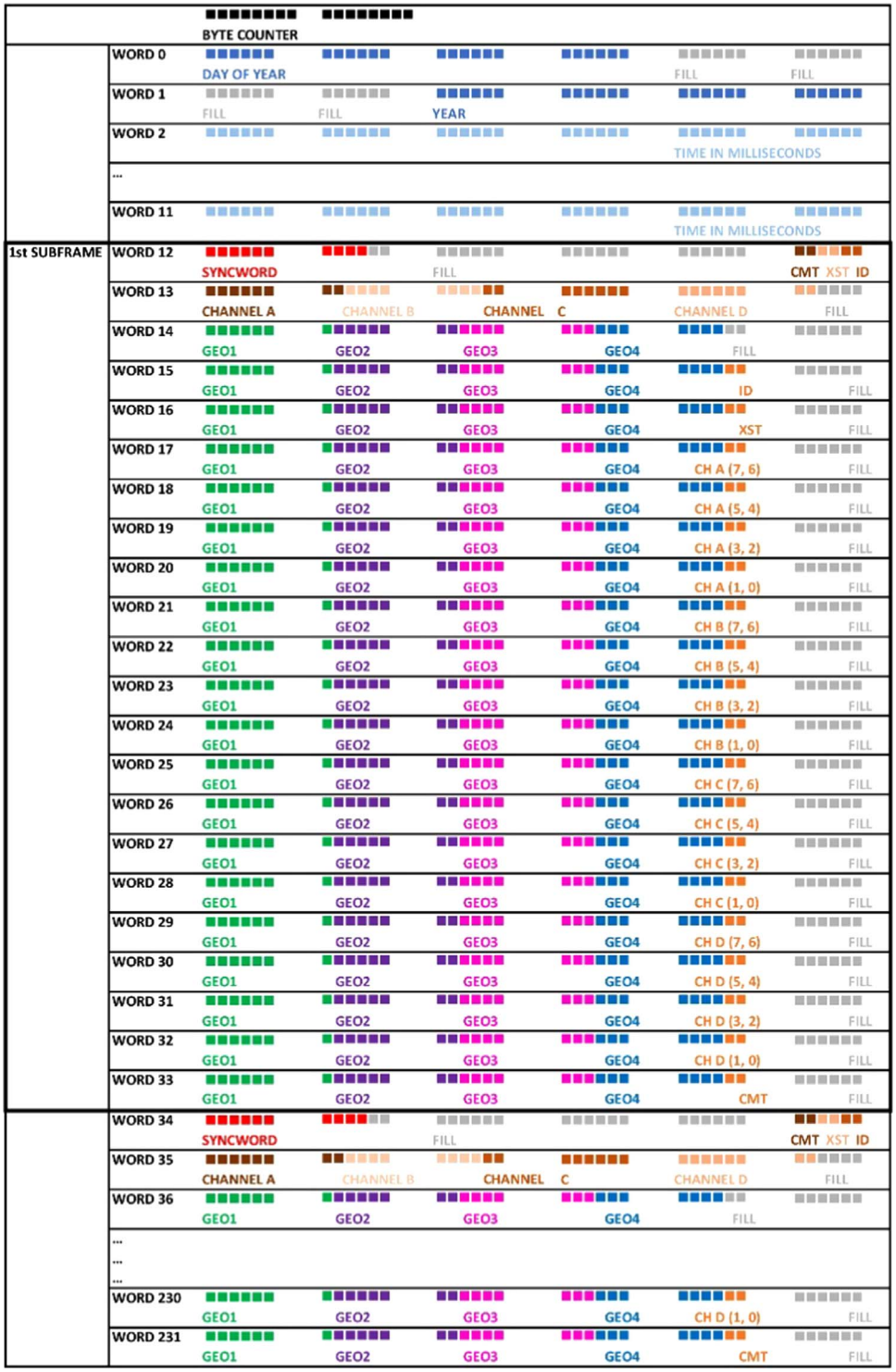

Fig. A 1. Scheme for deciphering original bit stream. Every box depicts one bit. 1 byte consists of 6 bits. Word 0 and 1 contain binary codes for day of year and year (dark blue boxes with filling zeros in light grey boxes). Words 2–11 contain time readings for the next 10 subframes. Every subframe starts with the synchronous word in red boxes and filling zeros are denoted in light grey boxes. Housekeeping data is depicted in this scheme with boxes in brownish colors. Geophone data is depicted in blocks of 7 bits as follows: geophone 1 in green boxes, geophone 2 in purple boxes, geophone 3 in pink boxes, and geophone 4 in blue boxes.

Appendix

Data format

The Apollo 17 LSPE recorded eight detonations of the explosive packages between December 15th and 18th, 1972. These signals were recorded on the Moon and transmitted as binary sequence to Earth (and handed over to the principal investigators for research). The original Apollo 17 LSPE data set “Seismic Profiling Active Listening Mode” can be ordered at NASA Space Science Data Center (NSSDC) using the ID-code PSPG-00021

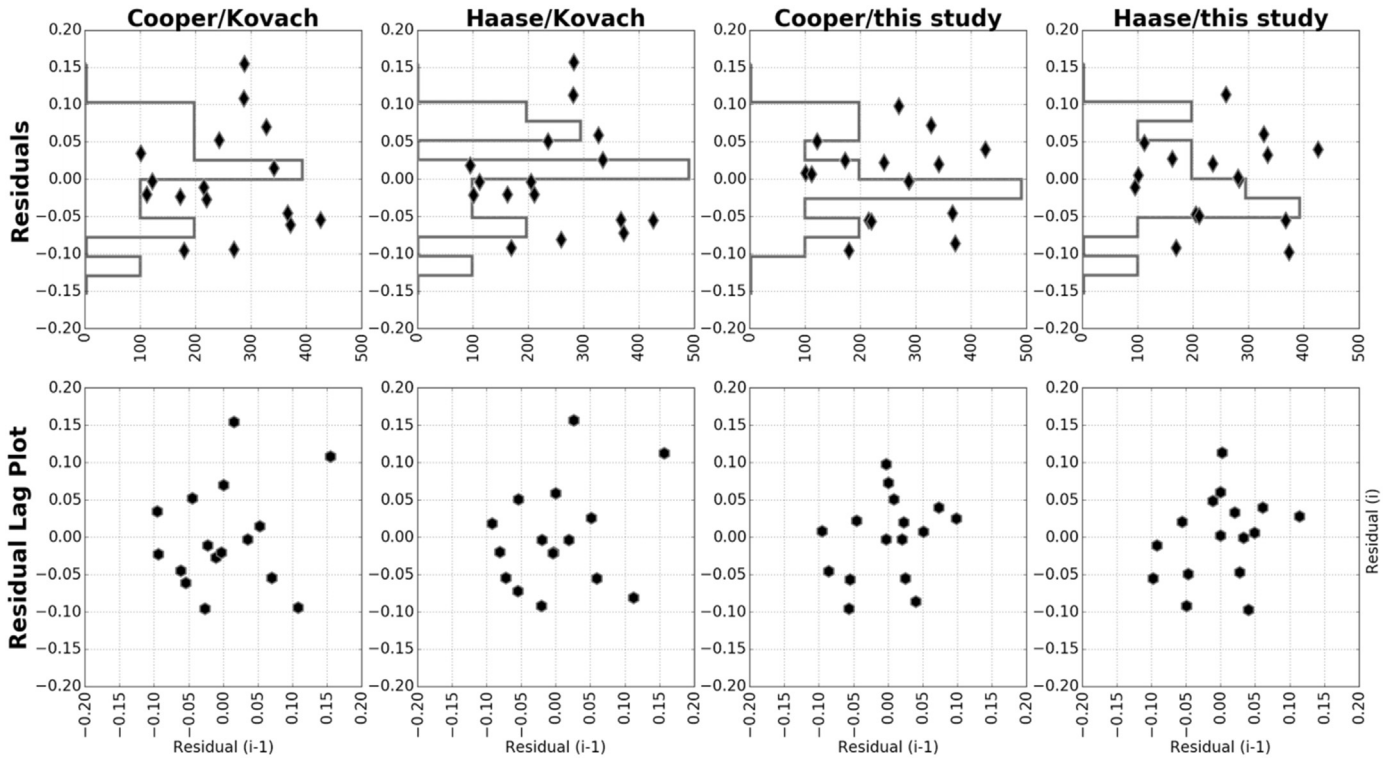

Fig. A 2. Residuals after model fits for the uppermost layers of two-layer case. Upper panels show residual plots of the four data sets with histogram plots of residuals in the background, lower panels show residual lag plots. Residual plots show a random pattern supporting a sufficiently accurate regression model for determining the slope. The normal distribution in histogram plots supports that. Residual lag plots show no identifiable structure, which means residuals are distributed randomly.

(http://nssdc.gsfc.nasa.gov/nmc/datasetDisplay.do?id=PSPG-00021). The provided data comprises the time span from 14-12-1972 to 18-12-1972, thus seismic data of all eight detonations and the impact of the LM decent stage are included. For this work we only used the detonation data.

The original data were stored on 7-track magnetic tape with a density of 800 characters per inch where 1 byte is 6 bits, which is in contrast to today's standards. Later, the data were restored and copied to 9-track magnetic tapes (6250 characters per inch) where 1 byte is 8 bits. To preserve the character nature of the data set, the 6 bits of each original character were put into the first 6 bits of an 8-bit byte and the next two bits of the 8-bit byte were filled with zeroes. This did not preserve the original bit stream. In addition, during restoration process a 2-byte counter was added every 1392 bytes indicating that 1392 bytes will follow in the next physical record. In order to recover the original bit stream it is necessary to remove the padded zeros and counting bytes.

The remaining data is written in non-fortran, binary buffered format with 36-bits per word, 232 words and ten subframes per record.

Word 0 contains the day of year decoded in the first four bytes and two bytes filled with zeroes. Word 1 contains two bytes of zeroes and the year in the last four bytes. Words 2–11 contain ten time strings for the following ten subframes, where the time is decoded as milliseconds of the day (straight binary up to 2^{36} milliseconds).

The first word of a subframe (e.g. word 12 in Fig. A1) contains the 10-bits synchronous word "00001110111″, 20 bits with filling zeroes, two bits of original subframe information, two bits for transmitter information, and two bits for geophone housekeeping data. The second word of a subframe (e.g. word 13 in Fig. A1) contains the unpatched channel information, which is displayed in bits 29 and 30 in the following 20 words (e.g. word 14–33 in Fig. A1) and four bits of filling zeroes. The channel information is still in bits 29 and 30 on each data word. The following 20 words contain the geophone data. In each data word, geophone data is written in 7-bit-blocks, so the first seven bits contain data of geophone 1, followed by 7 bits for geophone 2, 3, and 4. Then, in bits 29 and 30 parts of the channel information from the second word of the subframe can be found (as mentioned before). The last 6 bits of every data word are filled with zeroes. After that, the next subframe begins (Fig. A1).

Timing errors

As mentioned before, the signals from the lunar surface were transmitted in real time to Earth. There, they were received by range stations from the NASA Deep Space Network (DSN) which were distributed around the world. At these range stations, the signals were written on magnetic tapes together with a standard time signal. Time stamps on the tapes represented the time when the signal was received on Earth, not the time when the data was received by the lunar instruments. Then the data was written on another tape set for Principal Investigator (PI) use. Sometimes, when problems occurred in reading the standard time signal, the so-called "software clock" generated time stamps for the PI tapes. But these time stamps were extremely inaccurate and showed errors ranging from a fraction of a second to as much as a minute. Nakamura (2011) proved that the P-wave travel time for the Apollo 17 LM impact which were used to determine the deepest layer were in error, and therefore this layer can be neglected. Thus, the deepest layer of the study by Cooper et al. (1974) with a velocity of 4700 m/s was not considered in our study.

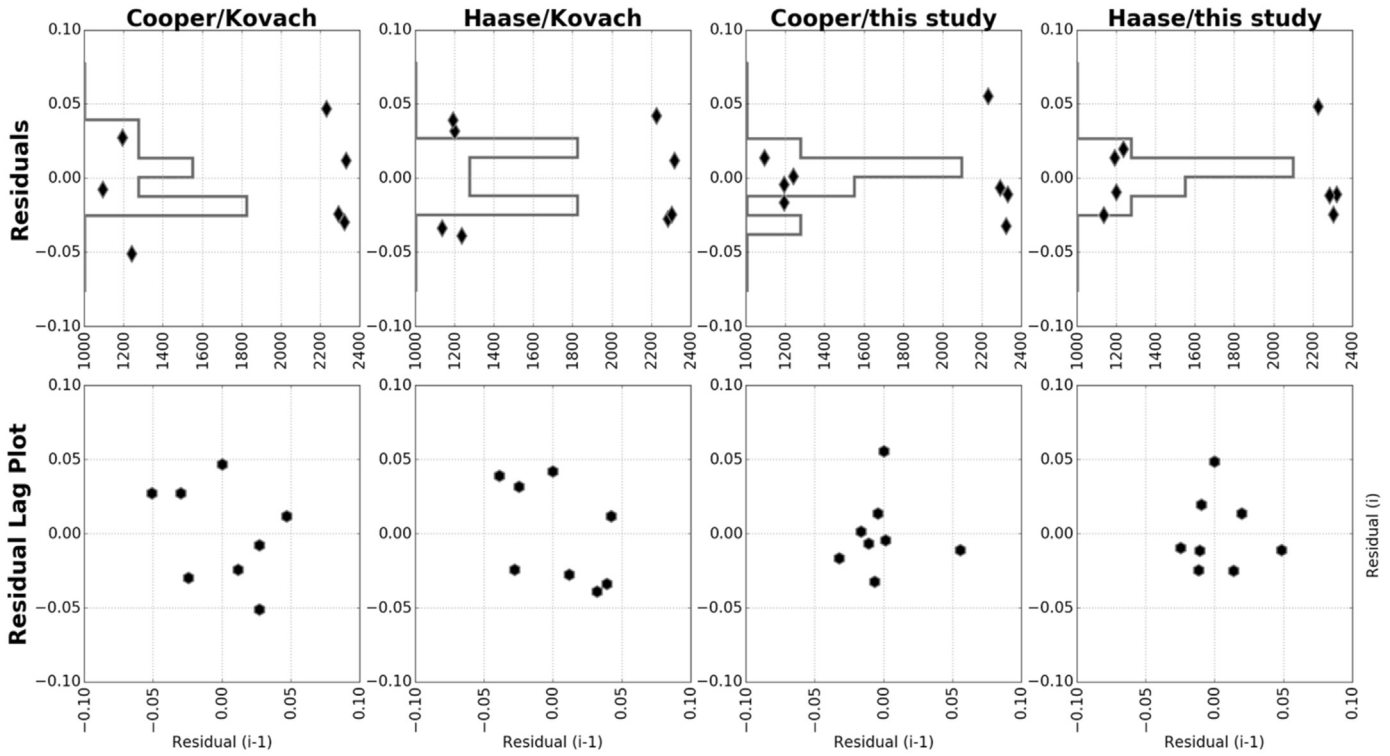

Fig. A 3. Residuals after model fits for the second layers of two-layer case. Upper panels show residual plots of the four data sets with histogram plots of residuals in the background, lower panels show residual lag plots. Residual plots show a random pattern supporting a sufficiently accurate regression model for determining the slope. The normal distribution in histogram plots supports that. Residual lag plots show no identifiable structure, which means residuals are distributed randomly.

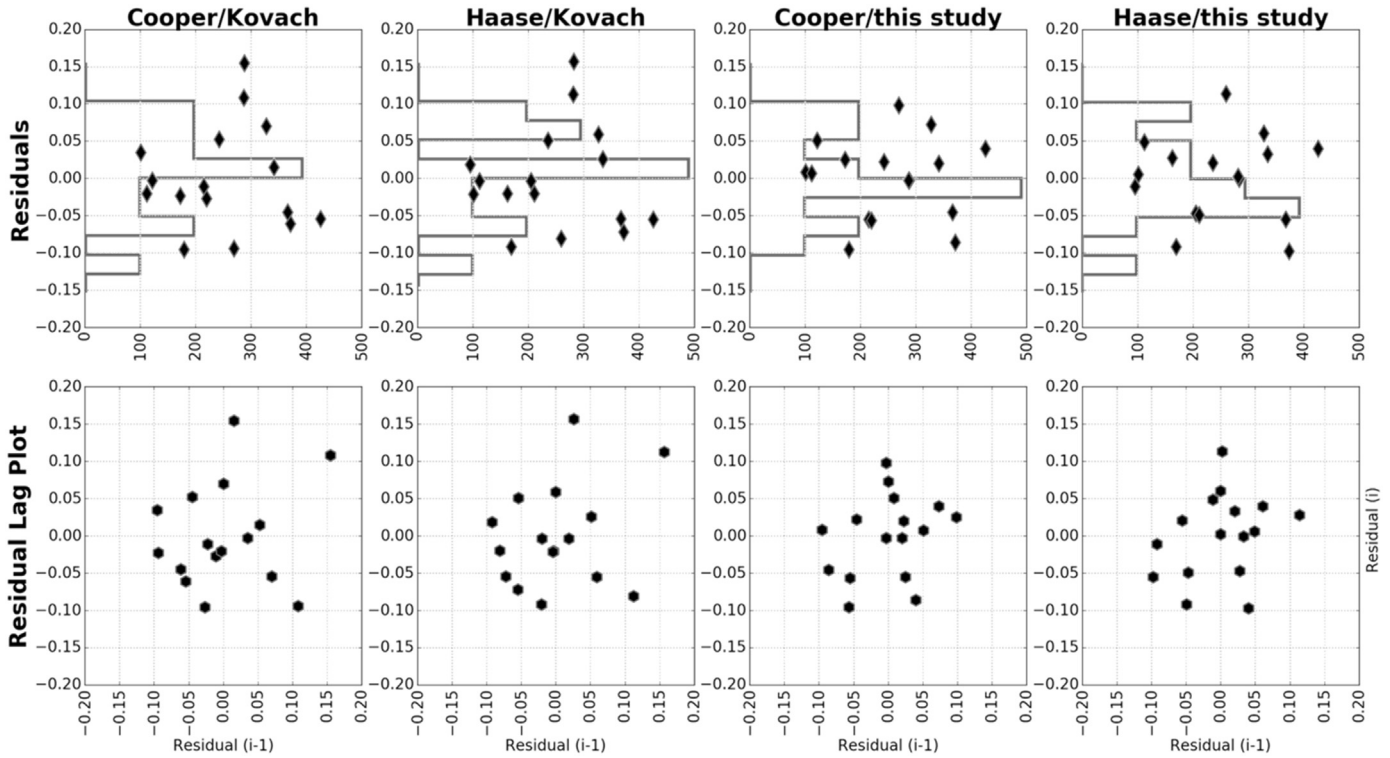

Fig. A 4. Diagrams for uppermost layers of three-layer case. Upper panels show residual plots of the four data sets with histogram plots of residuals in the background, lower panels show residual lag plots. Residual plots show a random pattern supporting a sufficiently accurate regression model for determining the slope. The normal distribution in histogram plots supports that. Residual lag plots show no identifiable structure, which means residuals are distributed randomly.

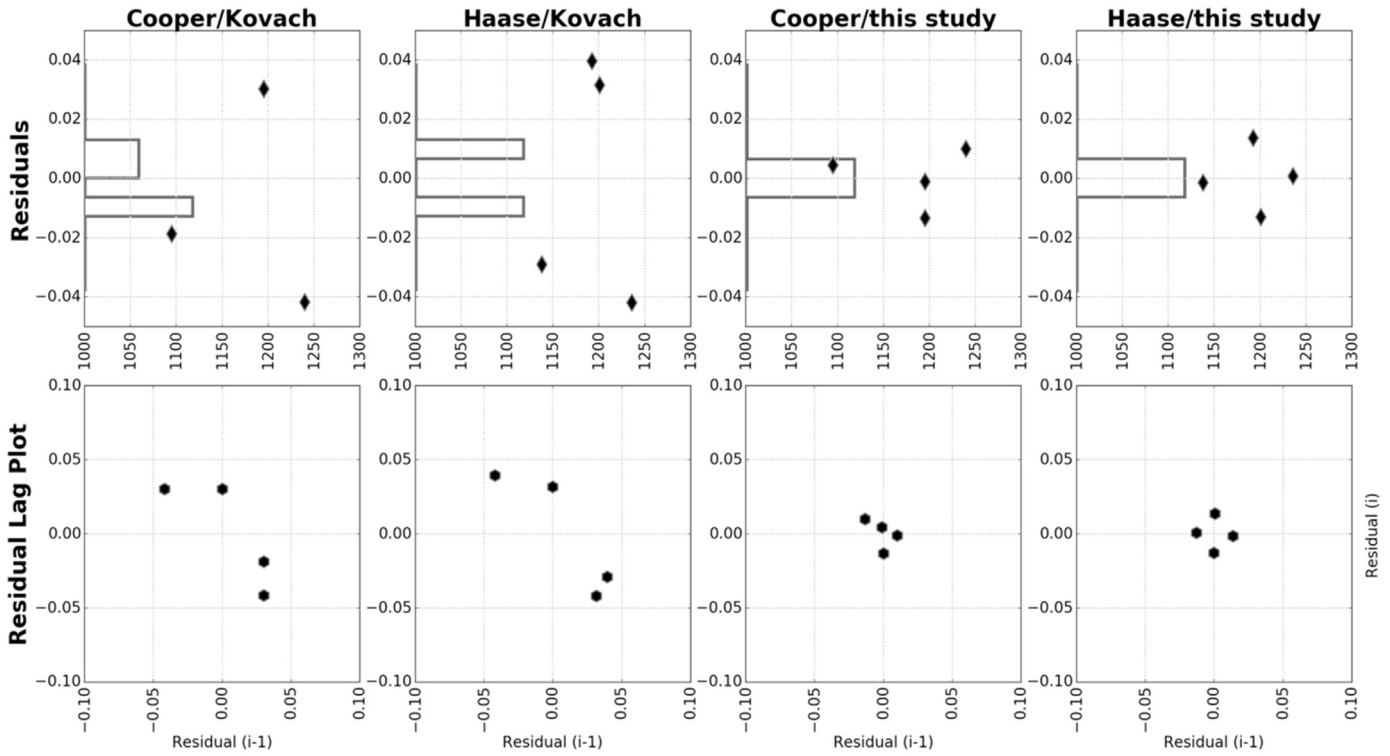

Fig. A 5. Diagrams for second layers of three-layer case. Upper panels show residual plots of the four data sets with histogram plots of residuals in the background, lower panels show residual lag plots. Residual plots show a random pattern supporting a sufficiently accurate regression model for determining the slope. The normal distribution in histogram plots supports that. Residual lag plots show no identifiable structure, which means residuals are distributed randomly.

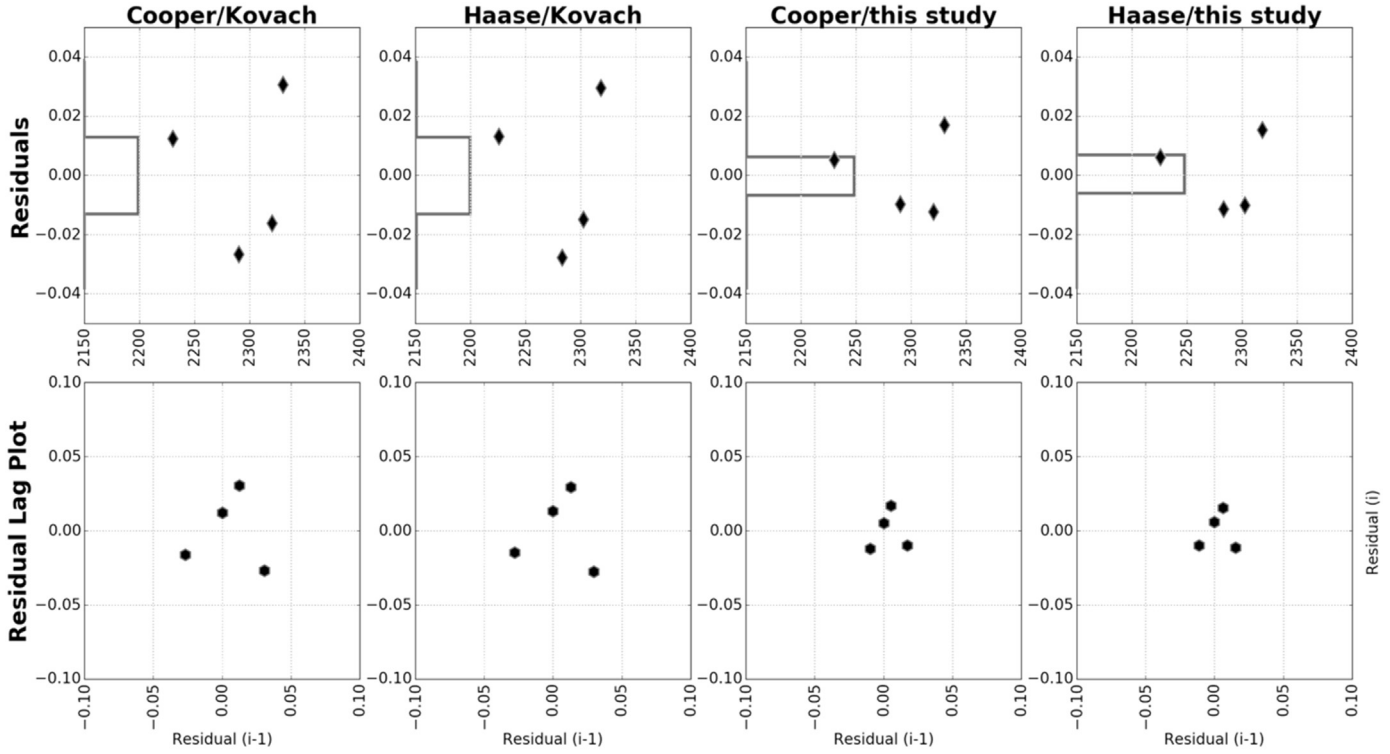

Fig. A 6. Diagrams for third layers of three-layer case. Upper panels show residual plots of the four data sets with histogram plots of residuals in the background, lower panels show residual lag plots. Residual plots show a random pattern supporting a sufficiently accurate regression model for determining the slope. The normal distribution in histogram plots supports that. Residual lag plots show no identifiable structure, which means residuals are distributed randomly.

Table A1
Detonation Times of Explosive Packages (from Apollo Scientific Experiments Data Handbook, 1974)).

Charge No.	Explosive Weight, g (lb)	Date, 1972	Time, G.m.t.
EP6	454 (1)	Dec. 15	23:48:14.56
EP7	227 (1/2)	Dec. 16	02:17:57.11
EP4	57 (1/8)	Dec. 16	19:08:34.67
EP1	2722 (6)	Dec. 17	00:42:36.79
EP8	113 (1/4)	Dec. 17	03:45:46.08
EP5	1361 (3)	Dec. 17	23:16:41.06
EP2	113 (1/4)	Dec. 18	00:44:56.82
EP3	57 (1/8)	Dec. 18	03:07:22.28

Residual analysis

Two-layer case

See Figs A2 and A3 here.

Three-layer case

See Figs A4–A6 and Table A1 here.

Overview of point-distances and travel times

See Table A2 here.

Table A2
Distances and P-wave travel times.

Charge No.	Geophone No.	Distance source-receiver from (Cooper and Kovach, 1975)	Distance source-receiver from (Haase et al., 2013)	P-wave travel time from (Kovach, 2015)	P-wave travel time from this study
EP2	G1	327 m	327.4 m	1.19 s	1.202 s
	G2	425 m	425.6 m	1.38 s	1.526 s
	G3	371 m	372.9 m	1.20 s	1.204 s
	G4	366 m	367.2 m	1.20 s	1.226 s
EP3	G1	242 m	236.3 m	0.90 s	0.843 s
	G2	341 m	334.9 m	1.18 s	1.201 s
	G3	288 m	282.9 m	1.15 s	0.985 s
	G4	287 m	281.0 m	1.10 s	0.982 s
EP4	G1	269 m	259.5 m	0.84 s	1.017 s
	G2	172 m	162.4 m	0.60 s	0.591 s
	G3	215 m	205.4 m	0.75 s	0.667 s
	G4	220 m	210.9 m	0.75 s	0.684 s
EP5	G1	2230 m	2225.9 m	3.90 s	4.027 s
	G2	2330 m	2318.4 m	3.95 s	4.087 s
	G3	2290 m	2283.2 m	3.88 s	4.041 s
	G4	2320 m	2302.6 m	3.90 s	4.053 s
EP6	G1	1195 m	1200.7 m	3.00 s	2.646 s
	G2	1240 m	1236.1 m	2.96 s	2.721 s
	G3	1195 m	1192.3 m	3.00 s	2.658 s
	G4	1095 m	1138.2 m	2.88 s	2.550 s
EP8	G1	170 m	169.4 m	0.55 s	0.496 s
	G2	101 m	95.0 m	0.43 s	0.316 s
	G3	122 m	111.9 m	0.46 s	0.435 s
	G4	112 m	101.4 m	0.41 s	0.355 s

References

Cooper, M.R., Kovach, R.L., 1975. Energy, frequency, and distance of moonquakes at the Apollo 17 site. In: Proceedings of the Conference Paper presented at the Lunar and Planetary Science.

Cooper, M.R., Kovach, R.L., Watkins, J.S., 1974. Lunar near-surface structure. Rev. Geophys. 12 (3), 291–308.

Duennebier, F., Sutton, G.H., 1974. Thermal moonquakes. J. Geophys. Res. 79 (29), 4351–4363.

Haase, I., Gläser, P., Knapmeyer, M., Oberst, J., Robinson, M.S., 2013. Improved Coordinates of the Apollo 17 Seismic Profiling Experiment (LSPE) Components. In: Proceedings of the 44th Lunar and Planetary Science Conference (Paper presented).

Heiken, G., Vaniman, D., French, B.M., 1991. Lunar sourcebook: a user's guide to the Moon. CUP Arch..

Kilmer, E.E., 1973. Laboratory, N.O. Final Report for Explosives for Lunar Seismic Profiling Experiment (LSPE). NASA T-558A.

Kovach, R.L., 2015. Person communication.

Nakamura, Y., 2011. Timing problem with the Lunar Module impact data as recorded by the LSPE and corrected near-surface structure at the Apollo 17 landing site. J. Geophys. Res.: Planets, (1991–2012)(116(E12).

NASA Document, 1972. Apollo Lunar Surface Experiments Package. Apollo 17 ALSEP (ARRAY E) Familiarization Course Handout, NASA-CR-128636, September.

Telford, W.M., Geldart, L.P., Sheriff, R.E., 1990. Applied geophysics 2nd Edition. Cambridge University Press.

Vostreys, R., 1980. Data User's Note: Apollo seismological investigations. NASA STI/Recon (Technical Report N, 81, 17970).